Numerical Study of Shock-Turbulence Interactions in Variable Density Flows

Yifeng Tian, Farhad Jaberi

Department of Mechanical Engineering
Michigan State University
East Lansing, MI 48824
tianyife@msu.edu, jaberi@msu.edu

Daniel Livescu

Los Alamos National Laboratory
Los Alamos, NM 87545
livescu@lanl.gov

Zhaorui Li

Texas A&M University-Corpus Christi
Corpus Christi, TX 78412
zhaorui.li@tamucc.edu

ABSTRACT

The effects of a planar shock wave on isotropic multi-fluid turbulence are studied using turbulence-resolving shock-capturing simulations. This is an extension of the canonical Shock-Turbulence Interaction (STI) problem, involving significant variable density effects. The numerical method has been verified using a series of grid and LIA convergence tests, and is used to generate accurate post-shock turbulence data for a detailed flow study. Density effects on post-shock turbulent statistics are shown to be significant, leading to an increased amplification of turbulent kinetic energy (TKE). Eulerian and Lagrangian analyses show that the increase in the post-shock correlation between rotation and strain is weakened in the multi-fluid case. Similar to previous single-fluid results and LIA predictions, the shock wave significantly changes the topology of the turbulent structures, exhibiting a symmetrization of the joint PDF of second and third invariant of anisotropic velocity gradient tensor. In the multi-fluid case, this trend is much more significant and mainly manifested in the heavy fluid regions.

INTRODUCTION

The interaction between a normal shock wave and isotropic turbulence is an important fundamental problem that has been extensively studied. Understanding this problem is a prerequisite for modeling complex phenomena such as inertial confinement fusion (ICF), hypersonic combustion, or astrophysical explosions. Ribner (1954) proposed a theoretical model for the description of STI, in which Eulerian Rankine-Hugoniot equations were solved. In this theory, referred to as Linear Interaction Approximation (LIA), the pre-shock turbulence was assumed to be made of small amplitude disturbances, so nonlinear and viscous effects were excluded from the analysis. Early DNS study of shock-isotropic turbulence interaction by Lee *et al.* (1993) was limited to relatively low flow Mach numbers (1.2 or less), and showed reasonably good agreement with LIA when turbulent Mach number M_t was kept small. Jamme *et al.* (2002) and Mahesh *et al.* (1997) have also used DNS to study the effects of different upstream turbulence flow parameters on STI. Lee *et al.* (1997), Larsson & Lele (2009), Larsson *et al.* (2013) have conducted turbulence resolving simulations for different flow Mach numbers using a high order shock-capturing scheme, and found good agreement with LIA results for some of the statistics, like turbulent kinetic energy and vorticity variance at relatively low M_t. More recently, Ryu & Livescu (2014) have conducted shock resolving DNS for a wide range of parameters and have showed that DNS results converge to LIA when the ratio of shock width to Kolmogorov length scale becomes small, even at low upstream Reynolds numbers.

All of the above studies (and most of other relevant works not discussed here) were focused on STI for single-fluid flows. Recently, an accurate shock-capturing method was used to study the variable density effects by conducting multi-fluid STI simulations (Tian *et al.*, 2017). Such a flow addresses processes occurring in hypersonic combustion and other applications where strong density variations exist. Tian *et al.* (2017) have shown that at Atwood number $A_t = 0.28$, multi-fluid STI further enhances the amplification of TKE and the reduction of turbulent length scales. In this study, we further investigate the variable density effects on STI using the shock-capturing finite difference method based on a Monotonicity-Preserving (MP) scheme (Li & Jaberi, 2012). Results obtained from grid/Eulerian data and fluid particle/Lagrangian data concerning the structure of the strain rate tensor are presented in this paper.

The paper is organized as follows. The computational setup and numerical methods are described in the next section including both grid/Eulerian and particle/Lagrangian methods. The accuracy of the numerical methods is established using both grid convergence tests and LIA convergence tests. The effects of variable density on turbulent structure are studied by comparing the multi-fluid data with the canonical single-fluid data. Lagrangian analyses are then carried out to study the dynamics of the turbulent structure. Finally, the main conclusions of this paper are summarized in the last section.

COMPUTATIONAL SETUP AND NUMERICAL ACCURACY

In this study, the conservative form of the dimensionless compressible Navier-Stokes equations for continuity, momentum, energy, and scalar are solved numerically together with the perfect gas law using a high-order hybrid numerical method. The inviscid fluxes are computed by the fifth-order MP scheme as described in Li & Jaberi (2012). The scalar equations are also computed in their conservative forms using the MP scheme. The viscous fluxes are calculated by the sixth-order compact scheme (Lele, 1992). The 3rd-order Runge-Kutta scheme is used for time advancement. The Lagrangian statistics are extracted from the flow field by solving the Lagrangian particle equations. The cubic spline scheme, whose accuracy in fluid particle tracking has been studied in Yeung & Pope (1988), is used in the pre- and post- shock regions. Inside the shock wave, the Monotonic Cubic Hermite interpolation scheme is used to ensure monotonicity around the shock. More than 1.048 million

randomly distributed particles are considered to ensure statistical convergence.

The physical domain for the simulations considered in this paper is a box that has a dimension of 4π in the streamwise direction (denoted as x) and $(2\pi, 2\pi)$ in the transverse directions (denoted as y and z) as shown in figure 1 (a). The coordinate system is fixed with respect to the initial normal shock position so that the shock wave stays relatively stationary around $k_0 x = 0.0$ during the simulation, where k_0 is the peak wavenumber of the energy spectrum. A sponge layer is used at the end of the computational domain to prevent reflecting waves. In the transverse directions, periodic boundary conditions are used so that the flow can be assumed to be periodic and homogeneous in these directions. To provide inflow turbulence, a pre-generated isotropic turbulence box is superposed on the uniform mean flow with Mach number = 2.0 and convected into the domain at inlet using Taylor's hypothesis. The isotropic turbulence box is generated following Ristorcelli & Blaisdell (1997) with $k_0 = 4.0$ with a final $M_t = 0.1$. In this M_t range, Taylor's hypothesis is good for approximating spatial developing turbulence with a temporal developing turbulence (Lee *et al.*, 1992). The variable density (multi-fluid) effects arise from compositional variations, by correlating the density to an isotropic scalar field. The scalar field is initialized using a double-delta function with a peak wavenumber $k_s = 8.0$. The scalar field is then allowed to decay in the fully developed isotropic turbulence simulation for one eddy turn over time following the passive scalar equation. The mass fractions of the two fluids can be extracted from the density field using the infinite speed of sound relation (Livescu & Ristorcelli, 2007; Livescu, 2013), which is approximately satisfied at low turbulent Mach numbers. The Atwood number corresponding to the molar weights of the two fluids is 0.28. This value of the Atwood number was chosen such that the variable density effects are non-negligible, yet the interaction with the shock wave is still in the wrinkled-shock regime. The Prandtl and Schmidt number are the same and equal to 0.75. The mean flow Mach number is 2.0. The turbulent Mach number and the Reynolds number based on the Taylor micro length scale are 0.09 and 45 right before the shock wave.

Table 1. Details of the mesh used in the grid convergence tests

	Mesh info	$\Delta x_d/\Delta y$	$(k_{max}\eta)_{min}$	η/δ_n
Grid-1	1024×256^2	2.0	0.96	0.93
Grid-2	1024×384^2	1.3	1.45	0.93
Grid-3	1536×384^2	2.0	1.45	1.40
Grid-4	1536×512^2	1.5	1.93	1.40
Grid-5	2048×512^2	2.0	1.93	1.86

Before discussing our main results, the procedure to obtain the statistics is described. In order to achieve statistical convergence, most statistics are spacially averaged over homogeneous (y and z) directions. Time averaging is also conducted for statistics which vary in the streamwise direction. All the results are obtained after the flow reaches the statistically steady state.

To verify the accuracy of our simulations, we have examined the turbulent statistics from two different perspectives. First, grid convergence tests are conducted to ensure that the statistics are grid converged and all turbulence scales are well-resolved. Two factors are considered in assessing the reliability of grid: a) the maximum turbulent wavenumber k_{max}, multiplied by the Kolmogorov length scale, η, should be considerably greater than one, and b) the scale separation between numerical shock thickness and η should be large enough (numerical shock thickness is calculated using $(\overline{u_{1,u}} - \overline{u_{1,d}})/|\partial u_1/\partial x_1|_{max}$, where $\overline{u_{1,u}}$ and $\overline{u_{1,d}}$ are the pre-shock and post-shock mean streamwise velocities) . Five different grids are used as shown in table 1. Results in figure 2 show that the turbulent statistics, including η and transverse vorticity variance, are grid-converged when the finest grid is used with $k_{max}\eta = 1.93$ and $\delta_n/\eta = 1.86$. Increasing either of these two values won't affect the post-shock turbulent statistics. The grey region in figure 2 (and any following figures) indicates the unsteady shock region, inside which the results are affected by the shock wrinkling and unsteady shock movement. Secondly, LIA convergence tests are conducted following Ryu & Livescu (2014) to show that the nonlinear and viscous effects can be correctly resolved using current numerical methods. A wide range of turbulent Mach numbers and Reynolds numbers is covered. Results show that shock-capturing simulation results do converge to LIA predictions for individual Reynolds stress components as long as certain conditions are satisfied. This is the first time that the asymptotic values for Reynolds stresses can be approximated using shock-capturing simulations.

RESULTS AND DISCUSSIONS

In this section, the results obtained from multi-fluid STI simulation are examined and compared with those of a reference single-fluid simulation case. In the reference case, the mass fraction of the heavy fluid is set to be 1.0. Other than the density field, the multi-fluid and the single-fluid simulations are similar. Re_λ and M_t are chosen to be 45 and 0.09 right upstream of the shock wave based on previous grid convergence and LIA convergence tests results.

Several low order post-shock turbulence quantities will be discussed first to give a general overview of the multi-fluid STI configuration. Figure 3 shows the density variance and TKE. Compared to the single fluid case, the multi-fluid case features large density variations before the shock wave ($k_0 x = 0.0$), which are mostly due to mixing of two fluids with different molecular weights. For the single-fluid case, only small density variations are generated by the turbulence. After the shock wave, the density variations are amplified, and this effect is much more manifested in the multi-fluid case. This amplification across the shock is related to intensified thermodynamic fluctuations. Immediately after the unsteady shock region (marked as grey in figure 3), multi-fluid density variations start to decrease, which is mainly related to the energy transition between acoustic and vorticity fields. After $k_0 \approx 2.0$, the decrease in density variance is slower, as the flow becomes dominated by turbulent mixing. For TKE shown in figure 3 (b), the amplification across the shock wave is also much stronger in the multi-fluid case, agreeing with our previous findings (Tian *et al.*, 2017). The peak TKE position shifts upstream to $k_0 x \approx 2.0$ in contrast to the single-fluid case which is at $k_0 x \approx \pi$. However, this shorter transient length in the multi-fluid case may not be universal, considering that it could be affected by the structure of density field, Atwood number and other flow parameters.

Variable density effects on shock modification of turbulent structure

In an earlier study on multi-fluid STI, we have focused on Reynolds stresses, vorticity variance, and turbulent length scales (Tian *et al.*, 2017) as the first quantities to examine and contrast with previous single-fluid STI studies. In Ryu & Livescu (2014); Livescu & Ryu (2015), the post-shock turbulence single-fluid STI data generated using shock-resolving DNS and LIA formulas are

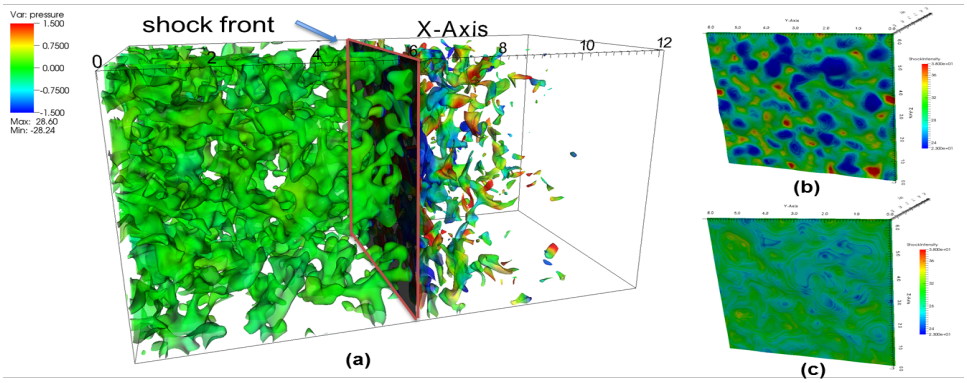

Figure 1. Instantaneous contours of 3D pressure fluctuations and shock surface in isotropic turbulence interacting with a Mach 2 shock. (*a*) The iso-surface of heavy fluid mole fraction ($\phi = 0.25$) is colored by instantaneous pressure fluctuations. The instantaneous shock surface is colored by the local pressure jump across the shock for (*b*) multi-fluid and (*c*) single-fluid cases.

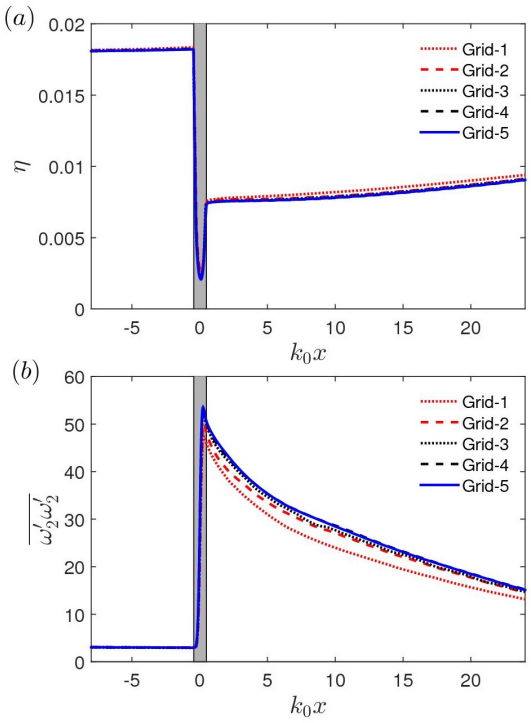

Figure 2. Results of multi-fluid grid convergence tests at $Re_\lambda = 45$ and $M_t = 0.09$. Streamwise development of (*a*) Kolmogorov length scale η and (*b*) transverse vorticity variance $\overline{\omega_2'\omega_2'}$ is shown. The region of unsteady shock movement is marked in grey.

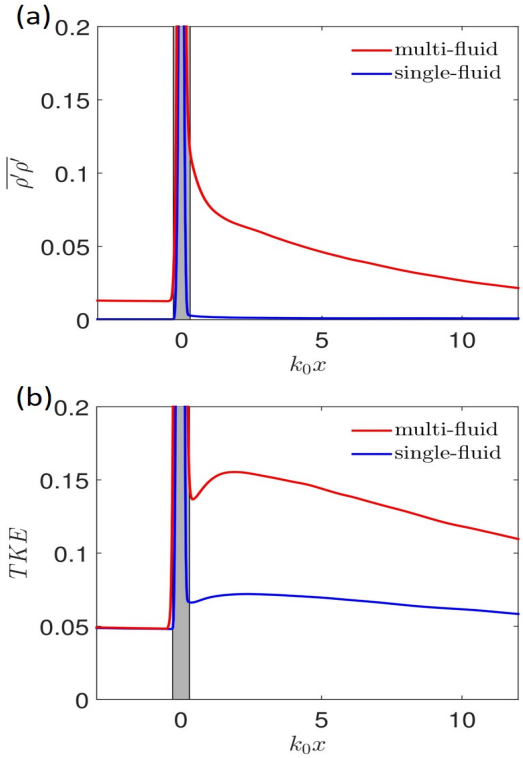

Figure 3. Plots of (*a*) density variance, (*b*) TKE for multi-fluid (red) and single-fluid (blue) simulations.

used to study the topological structure of turbulence. In this section, we aim to extend this analysis to multi-fluid STI to provide deeper understandings of the variable density effects on the turbulent structure.

The preferential amplification of the transverse components of the rotation and strain rate tensors is a well-known effect in STI and has been extensively studied for canonical single-fluid case in Mahesh *et al.* (1997); Ryu & Livescu (2014); Livescu & Ryu (2015). This can lead to an increase in the correlation between the two quantities. When density variations are introduced, Tian *et al.* (2017) showed that the transverse components of vorticity variance are further enhanced across the shock wave while the streamwise component retains almost the same values. To quantify the variable density effects on rotation and strain rate tensors, the PDF of the strain-enstrophy angle, Ψ, is shown in figure 4. Ψ is calculated using $\Psi = \tan^{-1}(S_{ij}S_{ij}/(W_{ij}W_{ij}))$, where $S_{ij} = 1/2(A_{ij} + A_{ji})$ and $W_{ij} = 1/2(A_{ij} - A_{ji})$ are strain and rotation tensors and $A = \nabla\overrightarrow{v}$ is the velocity gradient tensor. In isotropic turbulence, the PDF of Ψ peaks at 90° (Jaberi *et al.*, 2000), indicating a strain dominated structure. In single-fluid post-shock turbulence, the PDF of Ψ exhibits a shift of the peak from 90° to around 45°. This phenomenon has been observed by Livescu & Ryu (2015) and interpreted as the increase of the correlation between strain and rotation. In contrast, for the multi-fluid case, the peak still remains at the large angles and the increase in the correlated region is not as pronounced as that in the single-fluid case. This difference can also be observed in the joint PDF of $(W_{ij}W_{ij}/(W_{ij}W_{ij})_{max}, S^*_{ij}S^*_{ij}/(W_{ij}W_{ij})_{max})$ as shown in

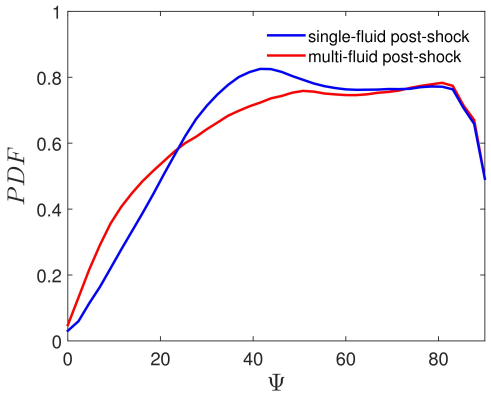

Figure 4. PDF of the strain-enstrophy angle Ψ in degrees for post-shock turbulence.

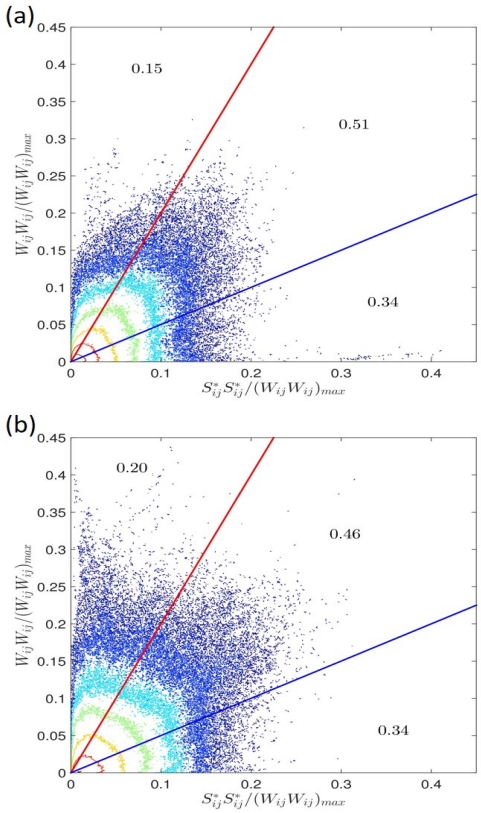

Figure 5. $\log_{10}$ PDF of $(W_{ij}W_{ij}/(W_{ij}W_{ij})_{max}, S^*_{ij}S^*_{ij}/(W_{ij}W_{ij})_{max})$ with iso-contour lines for (a) single-fluid case and (b) multi-fluid case. The regions of high rotation, high correlation, and high irrotational strain are separated by straight lines. The numbers indicate the probability of data points in the corresponding regions.

figure 5, where S^*_{ij} is the deviatoric strain rate tensor. The straight lines separate regions of high rotational strain ($W_{ij}W_{ij} > 2S^*_{ij}S^*_{ij}$), high correlation, and high irrotational strain ($W_{ij}W_{ij} < 0.5S^*_{ij}S^*_{ij}$). The single fluid case has an increased probability of correlated strain and rotation as expected. In the multi-fluid case (figure 5 (b)), there are less correlated structures and more high rotational structures compared to the single-fluid results, while the high irrotational structures remain approximatively the same. Figures 4 and 5 imply that the amplifications of the rotation and strain are affected differently when large density variations are present, which compromises the correlation between these two quantities.

To further characterize the turbulence structure behind the shock wave, we have performed an analysis of the invariant plane of the velocity gradient tensor. The second and third invariants (denoted as Q and R) of the anisotropic part of the velocity gradient tensor can reveal important details on the distribution of flow structures. The anisotropic part of the velocity gradient tensor is calculated using the formula $A^* = A - \theta/3I$, where $\theta = \nabla \cdot \overrightarrow{v}$. For isotropic turbulence, the joint PDF has the well-known teardrop shape which has been observed in boundary layers, mixing layers and channel flows (Pirozzoli & Grasso, 2004; Wang *et al.*, 2012). This type of distribution of Q and R indicates that for these flows, turbulence has a local topology of stable-focus/stretching or unstable-node/saddle/saddle. After the shock wave, Ryu & Livescu (2014) have shown, using LIA and DNS data that for single-fluid STI, that the shape of the distribution is significantly modified, demonstrating a symmetrization of the joint PDF. This symmetrization indicates that the regions with stable-focus/compression and stable-node/saddle/saddle (first and third quadrant) are enhanced. To understand the variable density effects on this symmetrization, the joint PDFs of (Q,R) are compared in figure 6.

Figure 6 (a) shows the joint PDF iso-contour lines for the single-fluid post-shock turbulence. The dashed lines denote the locus of zero discriminant of A^*, where Q and R satisfy $27R^2/4 + Q^3 = 0$. Compared to the pre-shock PDF (not shown), there is a tendency towards symmetrization of the invariant distribution, with more points located in the first and third quadrants. However, the trend is not as strong as those observed in Ryu & Livescu (2014). The reason is that the contours are shown in their linear scale, instead of the log-scale as in Ryu & Livescu (2014). When plotted in log scale, current results agree very well with those from previous DNS and LIA. The linear scale is here for better comparisons with the multi-fluid case. Similar to single-fluid STI, multi-fluid STI also demonstrates a tendency towards symmetrization of the (Q,R) distribution. However, the multi-fluid distribution is slightly more symmetric and has stronger variance, with more points away from the axes. This implies that more extreme turbulent structure events exist in the multi-fluid case. This also agrees with our previous study on multi-fluid STI that shows amplification of TKE to be stronger when there are significant variable density effects (Tian *et al.*, 2017). Another difference is that multi-fluid case shows more data points in the third quadrant, which correspond to the stable-node/saddle/saddle topology.

The density effects on the post-shock PDF of second and third invariants can be further explored by comparing the distribution of (Q,R) conditioned on regions with different densities. This is explored in figure 7 (a)-(c). Figure 7 (a) corresponds to the region of relatively high density ($\rho > (\overline{\rho} + 90\%\rho'_{rms})$), (b) to the region with density around the post-shock mean value, and (c) to the low density region ($\rho < (\overline{\rho} - 90\%\rho'_{rms})$). Before the shock wave, the PDFs corresponding to these regions are also compared and they are all very close to the single-fluid case (not shown). After the shock wave, the joint PDFs demonstrate significant differences between regions with different densities. Thus, in regions with density closer to that of post-shock mean density, the distribution of invariants appears to be very similar to that shown in figure 6. But for regions with higher density (figure 7 (a)), two important differences are observed. First, the joint PDF becomes more symmetric compared to those in the medium density region or single-fluid case. There is a much larger portion of data points having a local topology of stable-node/saddle/saddle. Secondly, less data points fall into first and second quadrants. On the other hand, post-shock regions with low density values exhibit characteristics similar to that of medium density

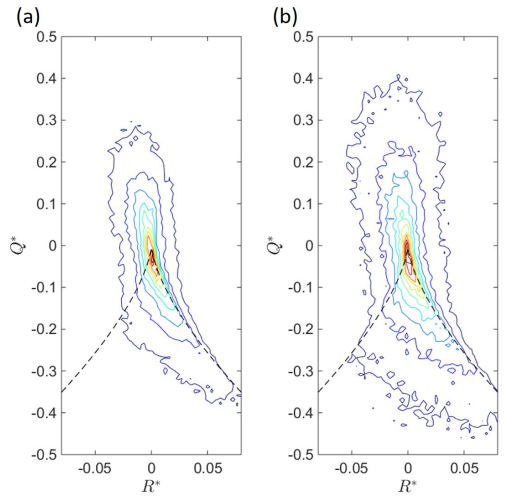

Figure 6. Iso-contour lines of joint PDFs of (Q,R), second and third invariant of and anisotropic part of the velocity gradient tensor for (a) single-fluid, (b) multi-fluid cases. The lateral lines denote the locus of zero discriminant.

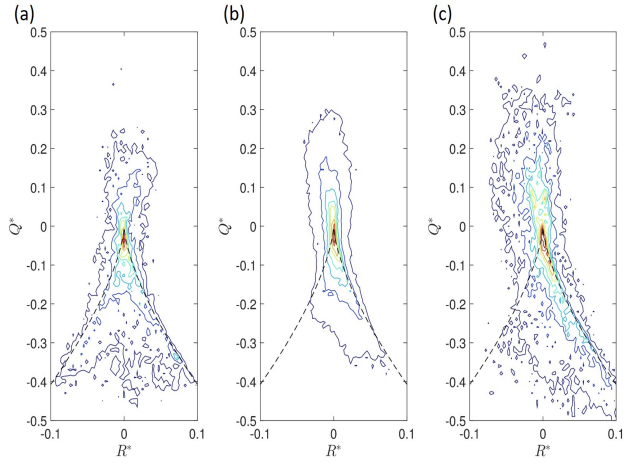

Figure 7. Iso-contour lines of post-shock ($k_0x = 0.44$) joint PDF of (Q,R), second and third invariant of and anisotropic part of the velocity gradient tensor in regions with different density values. (a,c) regions with high or low density values ($\rho > (\overline{\rho} + 90\%\rho'_{rms})$ or $\rho < (\overline{\rho} - 90\%\rho'_{rms})$), ($b$) regions with density around the post-shock mean value.

region. As can be seen in figure 7 (c), (Q,R) joint PDF in low density regions shows almost the same shape, only with a larger variance or wider distribution. The difference is hypothesized to be related to the stronger shock strength variation in the multi-fluid case. It was observed in the current study that the local shock strength is positively correlated with pre-shock density or post-shock density. With a stronger shock, the two-dimensionalization effect on post-shock turbulence is stronger in the high density region. For low density regions, the weaker two-dimensionalization effect reduces the trend of symmetrization. Moreover, the relatively lower inertia in these regions could make the return to isotropic turbulence process faster. The different characteristics of (Q,R) plane in regions with different densities provide additional evidence for the previous argument on density effects on preferential amplification of strain and rotation tensor.

Development of turbulence structure following fluid particles

In the previous section, we have shown that in multi-fluid STI, there is an enhancement of stable-node/saddle/saddle structure (3rd quadrant), especially in regions with relatively high density values. These data points can be extracted from the Eulerian results in a very straightforward manner. In order to also study the transient development of post-shock turbulence, one can examine the turbulent structure that follows the trajectory of fluid particles using Lagrangian data. The Lagrangian description of turbulence has been widely used in studying some important aspects of turbulence, such as particle dispersion, clustering and mixing. Non-inertial particles moving with the local flow velocity can shed light on transient processes, which are difficult to study using Eulerian data (Yeung, 2002). To the authors' knowledge, there has been no study of the history of the flow structures by following the trajectory of fluid particles in STI as has been done in other canonical turbulence problems (e.g. Nomura & Post (1998) for isotropic turbulence). In this study, we would like to show some preliminary results on the development of turbulent structures in a Lagrangian reference of frame, with the hope of providing basic understanding on the dynamics and statistical results for validation of dynamical models.

For the current simulations, we have tracked more than 1.088 million particles that are initialized uniformly at the same streamwise position right before the shock wave (like a sheet of particles), and calculated the turbulent structures following their trajectories. The aim is to show the history of the data points that fall into the 3rd quadrant in the joint PDF of second and third invariants, because this is an important feature of post-shock turbulence in STI, which is different than classical isotropic turbulence. Figure 8 shows the joint PDFs at different locations for the fluid particles that fall into the third quadrant right after the shock wave. All fluid particles are initially located before the shock wave at $k_0x \approx -0.6$. After the shock wave, the local topology of these particles is modified by the shock and part of them falls into the 3rd quadrant in the joint PDF shown in figure 6 (a). This portion of the particles are then labeled and tracked both upstream and downstream to examine the time development of the corresponding structures.

Figure 8 (a) shows the joint PDF of (Q,R) at the pre-shock position for the labeled particles. It is interesting to see that these particles have the classical tear-drop shape joint PDF. This implies that the modification of local turbulent structures through the shock wave is not strongly correlated with the pre-shock structure. It appears that the shock wave effects dominate over the history effects. This point is similar to our previous argument that the density (or varying shock strength) plays an important role in the change of local topology. After $k_0x \approx 0.44$, the development of the turbulent structures of the labeled particles is shown in figure 6 (b,c). At $k_0x \approx 0.88$, the labeled particles start to shift from the third quadrant to fourth quadrant. Further downstream at $k_0x \approx 2.09$ (around the post-shock peak TKE position), around half of the particles have a local topology of unstable-node/saddle/saddle (fourth quadrant). At the same time, the transition to the upper plane of the PDF (first or second quadrant) is very slow compared to that to the fourth quadrant.

CONCLUSIONS

The interaction of isotropic turbulence with a normal shock wave is studied using accurate shock-capturing turbulence-resolving simulation with a Lagrangian particle tracking algorithm. The main objective of this paper is to study the variable density effects by comparing multi-fluid STI with the single-fluid case. The numerical accuracy of the algorithm is established by performing both grid and LIA convergence tests. The results show that the tur-

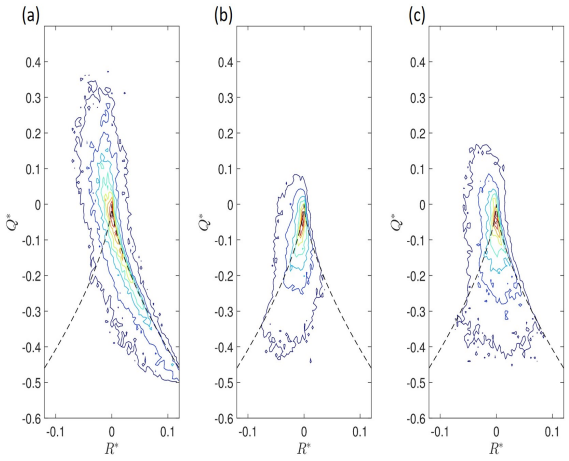

Figure 8. Iso-contour lines of pre-shock and post-shock joint PDF of (Q,R) at various locations. The data points are extracted following the same particles who fall into the 3rd quadrant in the joint PDF at $k_0 \approx 0.44$. (a) the joint PDF when the particle are traced upstream before the shock wave, (b,c) the joint PDF when the particles are traced downstream to $k0x \approx 0.88$ and $k_0x \approx 2.09$.

bulence statistics are grid-converged and the LIA prediction can be approached by varying either M_t or Re_λ, indicating good accuracy of the current numerical method.

Low order statistics are discussed first to show the variable density effects on STI. The multi-fluid case exhibits intensified density variations and TKE after the shock wave. A shorter transient region before the peak is also observed for multi-fluid TKE. The preferential amplification of rotation and strain rate tensors is affected by density variations and leads to a weaker correlation between the two quantities in the multi-fluid case. The variable density effects on turbulent structures are then examined by comparing the joint PDF of the second and third invariants of the velocity gradient tensor. The pre-shock joint PDF has the classical tear-drop shape. However, after the shock wave, a tendency towards symmetrization of the joint PDF, as in single-fluid STI, is observed for the multi-fluid case, with more data points falling into the third quadrant. After conditioning the joint PDFs based on fluid density, a large difference among heavy, medium, and light fluid regions is observed. In the heavy fluid regions, the joint PDF becomes almost completely symmetrical with an increasing portion of data in third quadrant. In contrast, the majority of the light fluid data points actually have a similar distribution to that of the medium density region. Lagrangian particles are then used to track the development of these turbulent structures. The results show that for the data points in the third quadrant, there is no preferential distribution on the joint PDF originated before the shock wave. Further downstream, the particles from the third quadrant start to shift to the other quadrants, but the shifting is faster towards the fourth quadrant.

ACKNOWLEDGEMENTS

This work was performed under the auspices of DOE. YT and FAJ were supported by Los Alamos National Laboratory, under Grant No. 319838. Los Alamos National Laboratory is operated by Los Alamos National Security, LLC for the US Department of Energy National Nuclear Security Administration under Contract No. DE-AC52-06NA25396. Computational resources were provided by the High Performance Computing Center at Michigan State University and the Texas Advanced Computing Center at The University of Texas at Austin .

REFERENCES

Jaberi, F. A., Livescu, D. & Madnia, C. K. 2000 Characteristics of chemically reacting compressible homogeneous turbulence. *Phys. Fluids* **12** (5), 1189–1209.

Jamme, S., Cazalbou, J.-B., Torres, F. & Chassaing, P. 2002 Direct numerical simulation of the interaction between a shock wave and various types of isotropic turbulence. *Flow Turbul. Combust.* **68** (3), 227–268.

Larsson, J., Bermejo-Moreno, I. & Lele, S. K. 2013 Reynolds- and Mach-number effects in canonical shock-turbulence interaction. *J. Fluid Mech.* **717**, 293–321.

Larsson, J. & Lele, S. K. 2009 Direct numerical simulation of canonical shock/turbulence interaction. *Phys. Fluids* **21** (12), 126101.

Lee, S., Lele, S. K. & Moin, P. 1992 Simulation of spatially evolving turbulence and the applicability of taylors hypothesis in compressible flow. *Phys. Fluids A: Fluid Dynamics* **4** (7), 1521–1530.

Lee, S., Lele, S. K. & Moin, P. 1993 Direct numerical simulation of isotropic turbulence interacting with a weak shock wave. *J. Fluid Mech.* **251**, 533–562.

Lee, S., Lele, S. K. & Moin, P. 1997 Interaction of isotropic turbulence with shock waves: effect of shock strength. *J. Fluid Mech.* **340**, 225–247.

Lele, S. K. 1992 Compact finite difference schemes with spectral-like resolution. *J. Comput. Phys.* **103** (1), 16–42.

Li, Z. & Jaberi, F. A. 2012 A high-order finite difference method for numerical simulations of supersonic turbulent flows. *Int. J. Numer. Meth. Fl.* **68** (6), 740–766.

Livescu, D. 2013 Numerical simulations of two-fluid turbulent mixing at large density ratios and applications to the Rayleigh-Taylor instability. *Phil. Trans. R. Soc. A* **371**, 20120185.

Livescu, D. & Ristorcelli, J. R. 2007 Buoyancy-driven variable-density turbulence. *J. Fluid Mech.* **591**, 43–71.

Livescu, D. & Ryu, J. 2015 Vorticity dynamics after the shock–turbulence interaction. *Shock Waves* **26** (3), 241–251.

Mahesh, K., Lele, S. K. & Moin, P. 1997 The influence of entropy fluctuations on the interaction of turbulence with a shock wave. *J. Fluid Mech.* **334**, 353–379.

Nomura, K. K. & Post, G. K. 1998 The structure and dynamics of vorticity and rate of strain in incompressible homogeneous turbulence. *J. Fluid Mech.* **377**, 65–97.

Pirozzoli, S. & Grasso, F. 2004 Direct numerical simulations of isotropic compressible turbulence: Influence of compressibility on dynamics and structures. *Phys. Fluids* **16** (12), 4386–4407.

Ribner, H. S. 1954 Convection of a pattern of vorticity through a shock wave. *NACA TR-1164* .

Ristorcelli, J. R. & Blaisdell, G. A. 1997 Consistent initial conditions for the dns of compressible turbulence. *Phys. Fluids* **9** (1), 4–6.

Ryu, J. & Livescu, D. 2014 Turbulence structure behind the shock in canonical shock-vortical turbulence interaction. *J. Fluid Mech.* **756**, R1.

Tian, Y., Jaberi, F., Livescu, D. & Li, Z. 2017 Numerical simulation of multi-fluid shock-turbulence interaction. In *AIP Conference Proceedings*, , vol. 1793, p. 150010. AIP Publishing.

Wang, J., Shi, Y., Wang, L.-P., Xiao, Z., He, X. T. & Chen, S. 2012 Effect of compressibility on the small-scale structures in isotropic turbulence. *J. Fluid Mech.* **713**, 588–631.

Yeung, P. K. 2002 Lagrangian investigations of turbulence. *Annu. Rev. Fluid Mech.* **34** (1), 115–142.

Yeung, P. K. & Pope, S. B. 1988 An algorithm for tracking fluid particles in numerical simulations of homogeneous turbulence. *J. Comput. Phys.* **79** (2), 373–416.